J. Fluid Mech. (2010), *vol.* 643, *pp.* 495–507. © Cambridge University Press 2010
doi:10.1017/S0022112009992461

Radial boundary layer structure and Nusselt number in Rayleigh–Bénard convection

RICHARD J. A. M. STEVENS[1]†, ROBERTO VERZICCO[2] AND DETLEF LOHSE[1]

[1]Department of Science and Technology and J. M. Burgers Center for Fluid Dynamics,
University of Twente, PO Box 217, 7500 AE Enschede, The Netherlands

[2]Department of Mechanical Engineering, Universitá di Roma 'Tor Vergata',
Via del Politecnico 1, 00133 Roma, Italy

(Received 27 April 2009; revised 18 September 2009; accepted 23 September 2009)

Results from direct numerical simulation (DNS) for three-dimensional Rayleigh–Bénard convection in a cylindrical cell of aspect ratio 1/2 and Prandtl number $Pr = 0.7$ are presented. They span five decades of Rayleigh number Ra from 2×10^6 to 2×10^{11}. The results are in good agreement with the experimental data of Niemela *et al.* (*Nature*, vol. 404, 2000, p. 837). Previous DNS results from Amati *et al.* (*Phys. Fluids*, vol. 17, 2005, paper no. 121701) showed a heat transfer that was up to 30 % higher than the experimental values. The simulations presented in this paper are performed with a much higher resolution to properly resolve the plume dynamics. We find that in under-resolved simulations the hot (cold) plumes travel further from the bottom (top) plate than in the better-resolved ones, because of insufficient thermal dissipation mainly close to the sidewall (where the grid cells are largest), and therefore the Nusselt number in under-resolved simulations is overestimated. Furthermore, we compare the best resolved thermal boundary layer profile with the Prandtl–Blasius profile. We find that the boundary layer profile is closer to the Prandtl–Blasius profile at the cylinder axis than close to the sidewall, because of rising plumes close to the sidewall.

Key words: direct numerical simulation, plume dynamics, Rayleigh-Bénard convection, thermal and viscous boundary layers, turbulent convection

1. Introduction

Turbulent Rayleigh–Bénard convection (RBC), continues to be a topic of intense research (Ahlers, Grossmann & Lohse 2009; Lohse & Xia 2010). The system is relevant to numerous astrophysical and geophysical phenomena, including convection in the Arctic ocean, the Earth's outer core, the interior of gaseous giant planets and the outer layer of the Sun. Therefore RBC is of interest in a wide range of sciences, including geology, oceanography, climatology and astrophysics.

For given aspect ratio $\Gamma \equiv D/L$ (D is the cell diameter and L its height) and given geometry, the nature of RBC is determined by the Rayleigh number $Ra = \beta g \Delta L^3/(\kappa \nu)$ and the Prandtl number $Pr = \nu/\kappa$. Here, β is the thermal expansion coefficient, g the gravitational acceleration, and $\Delta = T_b - T_t$ the difference between the imposed temperatures T_b and T_t at the bottom and the top of the sample, respectively, and ν and κ are the kinematic viscosity and the thermal diffusivity, respectively.

---

† Email address for correspondence: r.j.a.m.stevens@tnw.utwente.nl

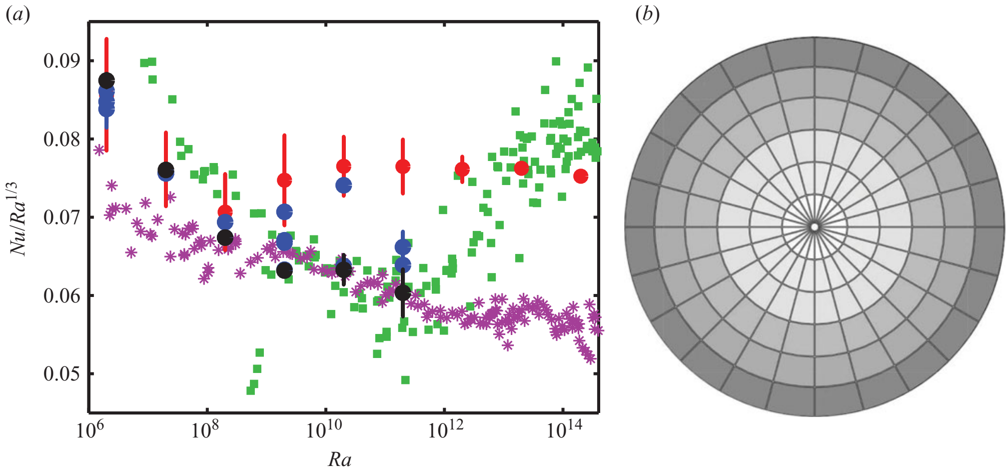

FIGURE 1. (*a*) Compensated Nusselt number versus the Rayleigh number for $Pr = 0.7$. Purple stars are the experimental data from Niemela *et al.* (2000), and the green squares are the experimental data from Chavanne *et al.* (2001). The DNS results from Verzicco & Camussi (2003) and Amati *et al.* (2005) are indicated in red, and the present DNS results with the highest resolution are indicated by the black dots. When the vertical error bar is not visible the error is smaller than the dot size. The results of the under-resolved simulations of this study are indicated by the blue dots. (*b*) Sketch of the grid geometry. The cells close to the sidewall are largest, and therefore this region is least resolved.

Experimental results are controversial (Heslot, Castaing & Libchaber 1987; Chavanne *et al.* 1997; Niemela *et al.* 2000, 2001; Roche *et al.* 2002; Niemela & Sreenivasan 2003; Funfschilling *et al.* 2005; Nikolaenko *et al.* 2005; Funfschilling, Bodenschatz & Ahlers 2009), so that the asymptotic behavior of $Nu(Ra)$ is yet unclear, and no generally accepted theory exists in that asymptotic regime (Kraichnan 1962; Spiegel 1971; Castaing *et al.* 1989; Shraiman & Siggia 1990; Grossmann & Lohse 2000, 2001, 2002; Lohse & Toschi 2003; Ahlers *et al.* 2009).

For more moderate Ra up to 2×10^{14} previous direct numerical simulation (DNS) by Amati *et al.* (2005) in a three-dimensional cylindrical cell of aspect ratio 1/2 with $Pr = 0.7$ showed a higher Nusselt number Nu than measured in experiments (see figure 1). In order to explain this discrepancy it was suggested by Verzicco & Sreenivasan (2008) that the experimental conditions are closer to fixed-heat-flux conditions than fixed-temperature boundary conditions of the horizontal plates. However, recent two-dimensional simulations by Johnston & Doering (2009) showed that Nu obtained in simulations with constant-temperature and constant-heat-flux boundary conditions are identical when $Ra \gtrsim 5 \times 10^6$. In this paper we show that the Nusselt number obtained in the three-dimensional simulations with constant-temperature boundary conditions is in good agreement with the experimental data (see figure 1) when the resolution is sufficiently high.

2. Numerical method and results on the Nusselt number

We numerically solved the three-dimensional Navier–Stokes equations within the Boussinesq approximation,

$$\frac{D\boldsymbol{u}}{Dt} = -\nabla P + \left(\frac{Pr}{Ra}\right)^{1/2} \nabla^2 \boldsymbol{u} + \theta \hat{z}, \tag{2.1}$$

$$\frac{D\theta}{Dt} = \frac{1}{(PrRa)^{1/2}}\nabla^2\theta, \tag{2.2}$$

with $\nabla \cdot \boldsymbol{u} = 0$. Here $\hat{z}$ is the unit vector pointing in the direction opposite to that of gravity; $D/Dt = \partial_t + \boldsymbol{u}\cdot\nabla$ is the material derivative; $\boldsymbol{u}$ is the velocity vector with no-slip boundary conditions at all walls; and θ is the non-dimensional temperature, $0 \leqslant \theta \leqslant 1$. The equations have been made non-dimensional by using the length L, the temperature Δ, and the free-fall velocity $U = \sqrt{\beta g \Delta L}$. The numerical scheme is described in detail in Verzicco & Orlandi (1996) and Verzicco & Camussi (1999, 2003).

The most important requirement for conducting DNS is to resolve all the relevant scales of the flow, i.e. the Kolmogorov length η and the Batchelor length η_T. According to Grötzbach (1983), the maximum wavenumber to be recorded by the grid is $k_{max} = \pi/h$, where $h = (\Delta x \Delta y \Delta z)^{1/3}$ is the mean grid width. This wavenumber must be greater than $1/\eta$, where $\eta = (\nu^3/\epsilon_u)^{1/4}$, and greater than $1/\eta_T$, where $\eta_T = (\kappa^3/\epsilon_u)^{1/4}$. According to Grötzbach (1983) this leads to the following restrictions on the mean grid widths:

$$h \leqslant \pi\eta \;=\; \pi(\nu^3/\epsilon_u)^{1/4} \text{ for } Pr \leqslant 1, \tag{2.3}$$

$$h \leqslant \pi\eta_T \;=\; \pi(\kappa^3/\epsilon_u)^{1/4} \text{ for } Pr \geqslant 1, \tag{2.4}$$

However the simulations presented in this paper show that it is necessary to properly resolve the flow in all directions of the flow. This means that the definition for h should read $h = \max(\Delta x, \Delta y, \Delta z)$. Note that this adapted criterion requires a higher resolution in the horizontal plane, especially in the boundary layers (BLs) close to the horizontal plates. This high resolution in the horizontal direction is necessary to properly resolve the plume dynamics in the BL, as the (thermal) gradients in this region are large in all directions of the flow and not only in the vertical direction. The simulations presented in this paper will show that it is crucial to properly resolve the plume dynamics to obtain accurate results for the Nusselt number.

When the vertical dissipation profile is assumed to be constant and is approximated by equating it to the production term due to buoyancy forces in the kinetic energy equation one obtains the following relations (Grötzbach 1983):

$$h \leqslant \pi\eta = \pi L \left(\frac{Pr^2}{RaNu}\right)^{1/4} \quad \text{for } Pr \leqslant 1, \tag{2.5}$$

$$h \leqslant \pi\eta_T = \pi L \left(\frac{1}{RaPrNu}\right)^{1/4} \quad \text{for } Pr \geqslant 1, \tag{2.6}$$

which are widely used in the literature. However one has to realize that RBC is anisotropic and that the dissipation rates strongly fluctuate in time and space. It is widely know that the dissipation rates peak close to the walls, and therefore there the relevant length scales are smallest. For DNS in a cylindrical geometry this means that one has to take care that the azimuthal resolution is sufficient, because the grid spacing $\Delta\phi$ is largest close to the sidewall, while the length scale that has to be resolved in that region is smallest. Furthermore, one has to realize that the dissipation rates strongly fluctuate in time and thus also the relevant length scales that have to be resolved (Schumacher, Sreenivasan & Yeung 2005). This means that when the relevant length scales in the simulation are determined from the azimuthally and time-averaged dissipation rate, the necessary resolution for a fully resolved simulation may locally or temporarily be even larger. How strong this effect is depends on the strength of the intermittency and therefore on the system parameters (Ra, Pr, Γ). Although relations (2.5) and (2.6) can be used to get an estimate of the required

Ra	$N_\theta \times N_r \times N_z$	Nu	Nu_h	Max-diff	N_{BL}	$\frac{\ell_{max,g}}{\eta}$	$\frac{\ell_{max,p}}{\eta}$	$\frac{\frac{\langle \epsilon_u \rangle}{\nu^3 Ra Pr^{-2}/L^4}+1}{Nu}$	$\frac{\frac{\langle \epsilon_\theta \rangle}{\kappa \Delta^2/L^2}}{Nu}$
2×10^6	$97 \times 49 \times 129$	*10.85*	*10.92*	*0.32 %*	*18*	*0.42*	–	–	–
2×10^6	$97 \times 49 \times 129$	10.68	10.32	0.35 %	18	0.42	0.51	0.973	0.978
2×10^6	$129 \times 65 \times 193$	10.56	10.86	0.15 %	27	0.31	0.39	0.972	0.986
2×10^6	$193 \times 97 \times 257$	11.02	11.03	0.44 %	35	0.21	0.26	0.974	0.991
2×10^7	$129 \times 49 \times 193$	*20.52*	*20.56*	*0.36 %*	*17*	*0.66*	–	–	–
2×10^7	$193 \times 97 \times 257$	20.54	20.69	0.70 %	31	0.46	0.64	0.989	0.987
2×10^7	$289 \times 129 \times 353$	20.64	20.53	0.36 %	42	0.34	0.43	0.984	0.991
2×10^8	$97 \times 49 \times 193$	40.57	40.71	0.02 %	10	1.84	2.82	1.007	0.926
2×10^8	$193 \times 65 \times 257$	39.42	39.52	0.02 %	13	0.92	1.41	0.992	0.950
2×10^8	$257 \times 97 \times 385$	39.41	39.10	0.79 %	19	0.70	1.11	0.995	0.973
2×10^9	$129 \times 65 \times 257$	89.07	88.25	0.02 %	6	3.01	4.57	1.001	0.858
2×10^9	*$193 \times 65 \times 257$*	*84.49*	*84.46*	*0.45 %*	*7*	*1.99*	*3.10*	*1.002*	*0.879*
2×10^9	$193 \times 65 \times 257$	84.10	83.66	0.51 %	7	1.98	3.06	1.000	0.877
2×10^9	$385 \times 97 \times 385$	79.75	78.70	0.70 %	10	1.15	1.47	0.999	0.935
2×10^9	*$513 \times 129 \times 513$*	*79.60*	*78.89*	*0.45 %*	*17*	*0.93*	*1.22*	*1.006*	*0.962*
2×10^{10}	$129 \times 97 \times 385$	201.08	201.21	1.01 %	12	6.56	10.88	1.006	0.878
2×10^{10}	$513 \times 129 \times 513$	171.79	169.58	2.09 %	19	1.59	2.83	0.994	0.927
2×10^{10}	$385 \times 257 \times 1025$	173.13	173.30	0.98 %	29	2.12	–	–	–
2×10^{11}	$769 \times 193 \times 769$	387.07	387.53	2.18 %	16	2.31	–	–	–
2×10^{11}	$769 \times 257 \times 1025$	373.64	368.88	2.03 %	18	2.28	6.34	0.9883	0.9058
2×10^{11}	$1081 \times 351 \times 1301$	352.67	364.75	4.15 %	26	1.60	3.96	1.0244	0.9318

TABLE 1. The columns from left to right indicate the following: Ra, the number of grid points in the azimuthal, radial and axial directions ($N_\theta \times N_r \times N_z$); the Nusselt number ($Nu$) obtained after averaging the results of the three methods (see the text) using the whole simulation length; the Nusselt number (Nu_h) after averaging the results of the three methods using the last half of the simulation; the maximum difference between the three methods (Max-diff); the number (N_{BL}) of points in the thermal BL; the maximum grid scale compared with the Kolmogorov scale estimated by the global criterion ($\ell_{max,g}/\eta$); and the maximum grid scale compared with the Kolmogorov scale estimated by the azimuthally and time-averaged dissipation rate. The last two columns give the Nusselt number derived from the volume-averaged kinetic $\langle \epsilon_u \rangle$ and thermal $\langle \epsilon_\theta \rangle$ dissipation rates compared with Nu indicated in the third column. The italic lines indicate a simulation started with a different initial flow field.

resolution, one has to realize that the result underestimates the resolution that is required to have a fully resolved simulation, because the fluctuations in time and space are not incorporated in these relations

All simulations in this paper are for $Pr = 0.7$, and therefore η is the smallest length scale in the flow. We simulated each Ra number on three different grids to test the influence of the grid scales. In table 1 the largest grid scale $\ell_{max} = \max(\Delta r, \Gamma L/2\Delta\phi, \Delta z)$ is compared with the Kolmogorov scale η for each simulation. We do this in two different ways; namely by looking at the global criterion (2.5), assuming a uniform distribution of the dissipation rates; see column ($\ell_{max,g}/\eta$) in table 1, and by estimating this ratio by looking at the time-averaged dissipation rates as a function of the position ($\ell_{max,p}/\eta$). Note that the relation between $\ell_{max,p}$ and $\ell_{max,g}$ shows that the global criterion indeed underestimates the required resolution for a fully developed DNS. The grid density near the plates has been enhanced to keep a sufficient number of nodes in the thermal BL, where the vertical temperature gradients are very high (see the column 'N_{BL}' in table 1). According to Grötzbach (1983) three points in the thermal BL should be sufficient. In the papers by Verzicco & Camussi (2003) and Amati *et al.* (2005) it has already been noted that more than three grid points in the thermal BL are required. Indeed, the results clearly show that more grid points in the thermal BL are required to have a fully developed simulation. As the number of points needed in the thermal BL increases with Ra because of the increasing strength of the turbulent fluctuations and the relation between η and λ_θ, we cannot give a strict universal criterion for the number of points that should be within the thermal BL. The strength of the plumes decreases slowly when the plumes travel further away from the plates, and therefore the grid spacing from the plates to the bulk has to be increased gradually to prevent the plumes from becoming under-resolved just above the thermal BL.

For all simulations up to $Ra = 2 \times 10^{10}$ on the $129 \times 97 \times 385$ grid we simulated the flow for at least 200 dimensionless time units (2 dimensional time units equal 1 turnover time) to make sure that the statistically stationary state has been reached and all transient effects are washed out; before we started to collect data for an additional 400 dimensionless time units (and some cases even for 3000 dimensionless time units) so that the statistical convergence could be verified. For simulations where the flow field obtained at a lower Ra (or a new random flow field) is used as an initial condition, we observe a small overshoot in Nu, before it settles to its statistically stationary value. The long initialization runs we used prevent this from influencing our results. This is double-checked by the convergence of the different methods we use to calculate Nu. Since most simulations are started from an interpolated field obtained at a lower Ra, we recomputed Nu for $Ra = 2 \times 10^9$ on the $193 \times 65 \times 257$ grid with a new flow field to rule out the effect of hysteresis on the obtained Nusselt number results. The result is shown in italics in table 1 and is in excellent agreement with the original result.

For the six most demanding simulations, i.e. the bottom five cases in table 1 and the simulation for $Ra = 2 \times 10^9$ on the $513 \times 129 \times 513$ grid, the criteria for time averaging had to be relaxed because of the limited CPU time available. Therefore we averaged these cases for 100 dimensionless time units (300 time units for the simulation at $Ra = 2 \times 10^{10}$ on the $385 \times 257 \times 1025$ grid, 200 dimensionless time units for $Ra = 2 \times 10^9$ on the $513 \times 129 \times 513$ grid and 40 dimensionless time units for $Ra = 2 \times 10^{11}$ on the $1081 \times 351 \times 1301$ grid). The simulations at $Ra = 2 \times 10^{10}$ have completely different initial conditions; i.e. different flow fields obtained at lower Ra are used as the initial condition. Nonetheless, we observe good agreement.

We calculate Nu as volume average and also by using the temperature gradients at the bottom and top plates. The volume average is calculated from the definition of the Nusselt number $Nu = (\langle u_z \theta \rangle_A - \kappa \partial_3 \langle \theta \rangle_A) / \kappa \Delta L^{-1}$ (Verzicco & Camussi 1999). In addition, we average over the entire volume and time. The value of Nu in table 1 gives the average value of the three methods, i.e. the volume average and the averages based on the temperature gradients at the bottom and top plates, for the simulation length of the actual simulation, which is normally 400 dimensionless time units. We also determined Nu over the last half of our simulations, normally the last 200 dimensionless time units (see the column 'Nu_h' in table 1). These values are within 1 % of the value determined over the whole simulation, showing that our results are well converged. The maximum difference in Nu obtained from the three methods, i.e. volume average and using the temperature gradients at the plates, is given in the column 'Max-diff' in table 1.

Figure 1 shows that the DNS data converge to the experimental data when the resolution is increased. The results indeed show that a very high resolution is required to obtain converging results for the Nusselt number. The error bars in figure 1 indicate the maximum of the following three quantities: (i) the maximum difference between the three methods to determine Nu; (ii) the difference between Nu determined over the whole simulation length and Nu determined over the last half of the simulation;

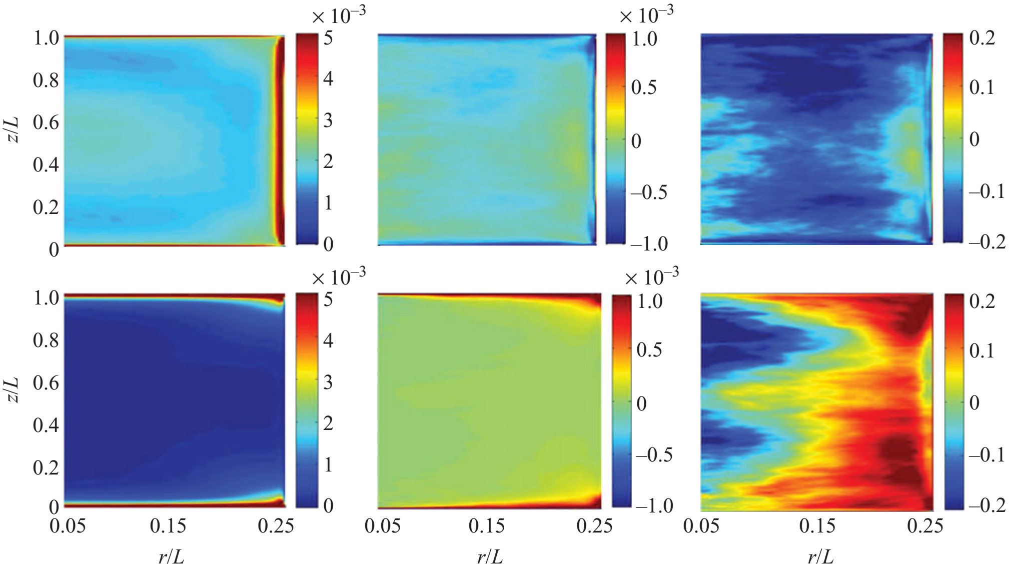

FIGURE 2. Dimensionless kinetic (upper plots) and thermal (lower plots) dissipation rates at $Ra = 2 \times 10^9$. The upper row gives $\widetilde{\epsilon}_u = \epsilon_u L^3/U^2$ and the lower row $\widetilde{\epsilon}_\theta = \epsilon_\theta U/(\Delta^2 L)$. The left column indicates the dimensionless kinetic $\widetilde{\epsilon}_u$ and thermal $\widetilde{\epsilon}_\theta$ dissipation rates for the high-resolution case ($385 \times 97 \times 385$). The middle column gives $\widetilde{\epsilon}_u^H - \widetilde{\epsilon}_u^L$ (upper plot) and $\widetilde{\epsilon}_\theta^H - \widetilde{\epsilon}_\theta^L$ (lower plot), where the superscripts H and L, respectively, mean the data obtained from the high- ($385 \times 97 \times 385$) and low-resolution simulations ($129 \times 65 \times 257$). The rightmost column gives $(\widetilde{\epsilon}_u^H - \widetilde{\epsilon}_u^L)/\widetilde{\epsilon}_u^H$ (upper plot) and $(\widetilde{\epsilon}_\theta^H - \widetilde{\epsilon}_\theta^L)/\widetilde{\epsilon}_\theta^H$ (lower plot). The difference for the thermal dissipation rates between the fully resolved and the under-resolved simulations is largest (in absolute values) close to the sidewall.

(iii) when the error bar based on criteria 1 and 2 is smaller than 1 % after averaging over 400 dimensionless time units the error is assumed to be 1 %. When the data are averaged over 100 dimensionless time units we take a minimal error of 3 %. For 2×10^6 and 2×10^7 we also determined the variation in Nu at various distances from the horizontal plates (Shishkina & Wagner 2007) and found that the differences are smaller than 0.2 %. We note that Nu fluctuates more in time than in space (after sufficient spatial averaging). This check also shows that the Nusselt number results in our simulation are well converged. The difference in Nu we get from independent simulations is normally well within these error margins when exactly the same grid is used, except for some cases at $Ra = 2 \times 10^6$.

3. Dissipation rates and temperature distribution functions

Another way to calculate Nu is to look at the two exact global relations for the volume-averaged kinetic and thermal energy dissipation rates $\langle \epsilon_u \rangle = \nu^3 (Nu - 1) Ra Pr^{-2}/L^4$ and $\langle \epsilon_\theta \rangle = \kappa \Delta^2 Nu/L^2$, respectively (Shraiman & Siggia 1990). We have calculated the azimuthally and time-averaged energy dissipation rate $\epsilon_u(\vec{x}) = \nu |\nabla \boldsymbol{u}|^2$ and the thermal dissipation rate $\epsilon_\theta(\vec{x}) = \kappa |\nabla \theta|^2$. Figure 2 compares the difference between the dissipation rates obtained in the fully resolved and the under-resolved simulations and reveals a higher thermal dissipation rate for the fully resolved simulations, as it is calculated from the (temperature) gradients. In the under-resolved simulations the gradients are smeared out, and therefore ϵ_u and ϵ_θ are underestimated. To check the resolution, we calculated ϵ_u and ϵ_θ from the respective gradients and compared them with the values obtained from the above-given global exact relations. Table 1 shows that for ϵ_u the relation is basically satisfied for all simulations, whereas for ϵ_θ the difference can be considerable. For higher Ra numbers the temperature field is under-resolved because of the line structure of the plumes very close to the horizontal plates and close to the sidewalls. Since the thermal dissipation rate in these regions is much higher than the kinetic dissipation rate this effect is much more pronounced in the convergence of the thermal dissipation rate than in the convergence of the kinetic dissipation rate. We note that the value for the Nusselt number seems to be converged earlier than the convergence of the dissipation rates. Testing above exact relations seems to be the best way to verify the grid resolution. For 2×10^6 and 2×10^7 the kinetic dissipation rate is not converged because we cannot properly resolve the kinetic dissipation rate close to the cylinder axis due to the metric factors $1/r$, $1/r^2$, ... that amplify the numerical errors in the squared gradients in this region. At higher Ra the fraction of the kinetic dissipation that is in this region is smaller, and therefore the convergence is better.

The vertical heat flux concentrates in the plume-dominated sidewall region in which the vertical velocity reaches its maximum (Shang, Tong & Xia 2008). Therefore it is very important to properly resolve the region close to the sidewall. However, figure 2 reveals that in the under-resolved simulations the region close to the sidewall is least resolved (red areas in the plot where the thermal dissipation rates are compared, right plot), as there the finite volumes are largest, because of the cylindrical geometry of the grid (see figure 1*b*). When the resolution is insufficient close to the sidewall, the plumes in this region, which are important for the heat transfer, are not properly resolved and not sufficiently dissipated. Therefore too much heat is transported across the cell, leading to an overestimation of Nu in the under-resolved simulations. Furthermore, figure 2 shows that the thermal dissipation rate in the under-resolved simulations is overestimated in the central region. This is due to the flow organization at higher Ra; see figure 8 of Verzicco & Camussi (2003), where it is shown that there is a double convection roll for $Ra = 2 \times 10^9$. Because the plumes close to the sidewall are insufficiently dissipated in the under-resolved simulations the plumes that will reach the central region of the cell will be stronger in the under-resolved simulations than in the better-resolved ones. This leads to a higher dissipation in the central region in under-resolved simulations with respect to better-resolved simulations. Supplementary movies (available for viewing at journals.cambridge.org/flm) reveal the dynamics of the system for the different grid resolutions. Movie 1 shows the temperature field in horizontal cross-sections close to bottom plate and movie 2 that at mid-height. Note that the coarseness of the under-resolving grids does not capture all the characteristics of the flow observed in the high-resolution simulation.

To further investigate the influence of the grid resolution, we calculated the azimuthally averaged probability density functions (p.d.f.s; see also Emran & Schumacher 2008; Kunnen *et al.* 2008; Shishkina & Wagner 2007, 2008; Kaczorowski & Wagner 2009) of the temperature averaged over 3000 dimensionless time units for $Ra = 2 \times 10^8$, comparing the under-resolved case ($97 \times 49 \times 193$) with the fully resolved one ($193 \times 65 \times 257$). Figure 3 shows that the temperature p.d.f.s at mid-height and at a distance λ_θ^{sl} (thermal BL based on the slope) from the plates have longer tails in the under-resolved simulation than in the better-resolved one. Again the reason lies in the rising (falling) plumes from the bottom (top) plate, which are not properly dissipated in the under-resolved simulations and therefore travel further from the plates. The comparison with the p.d.f. obtained using half of the time series reveals that the differences in the p.d.f.s are not due to a lack of averaging but are due to insufficient grid resolutions. We note that we observe similar differences at other

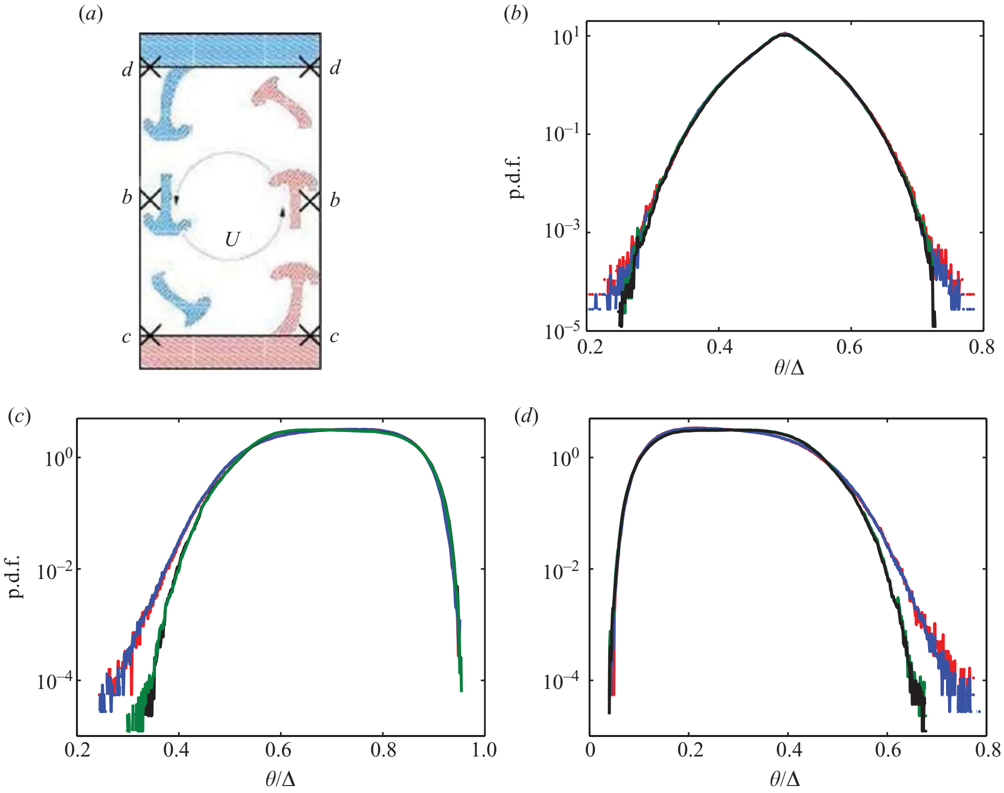

FIGURE 3. (*a*) A sketch showing the locations (crosses) of the azimuthally averaged temperature p.d.f.s, shown in panel (*b*), panel (*c*) and panel (*d*), for $Ra = 2 \times 10^8$ obtained on different grids. The radial position is $0.2342L$ for the under-resolved ($97 \times 49 \times 193$) and $0.2314L$ for the better-resolved ($193 \times 65 \times 257$) simulations. The temperature p.d.f. for the better-resolved simulations averaged over 3000 dimensionless time units is indicated in black. The green line indicates the result using half of the time series. The temperature p.d.f. averaged over 3000 dimensionless time units for the under-resolved simulations is indicated in blue, and the red indicates the result using half of the time series. (*b*) Temperature p.d.f. at mid-height. (*c*) Temperature p.d.f. at the distance λ_θ^{sl} from the bottom plate. (*d*) Temperature p.d.f. at the distance λ_θ^{sl} from the top plate.

radial positions; only the averaging around the cylinder axis ($r = 0$) leads to results that are not fully converged because of the cylindrical geometry. In figure 4 we show the effect of the grid resolution on the flatness $F = \langle(\theta - \langle\theta\rangle)^4\rangle / \langle(\theta - \langle\theta\rangle)^2\rangle^2$ obtained at mid-height for the better-resolved and under-resolved simulations. Comparison between the solid and dashed lines shows that the data are converged close to the sidewall, where the statistics is best because of geometric reason. Comparison between the black (well resolved) and red (under-resolved) lines reveals that the insufficiently dissipated plumes mainly close to the sidewall leads to too-large flatnesses in the under-resolved simulations.

4. Boundary layers

Although the bulk is turbulent, scaling-wise the BLs still behave in a laminar way because of the small BL Reynolds number (Ahlers *et al.* 2009). In figure 5 we compare the thermal BL profile obtained from the simulations with the Prandtl–Blasius (PB) profile, as done by Sugiyama *et al.* (2009) for two-dimensional Rayleigh–Bénard

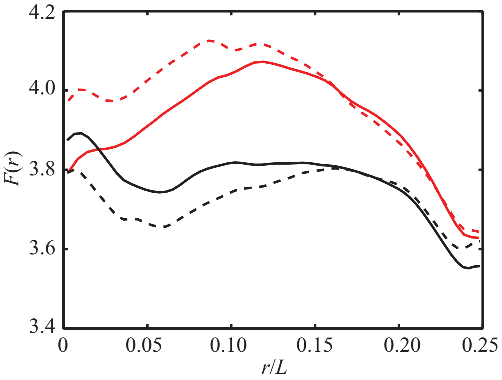

FIGURE 4. Flatness of the temperature p.d.f. at mid-height for $Ra = 2 \times 10^8$ for the under-resolved (red, $97 \times 49 \times 193$) and the better-resolved (black, $193 \times 65 \times 257$) simulations. The solid lines indicate the result after averaging over 3000 dimensionless time units and the dashed lines the result after averaging over 1600 dimensionless time units. Both simulations are started from the same initial field obtained at a lower Ra, and the data collection is started when each simulation has reached the statistically stationary state.

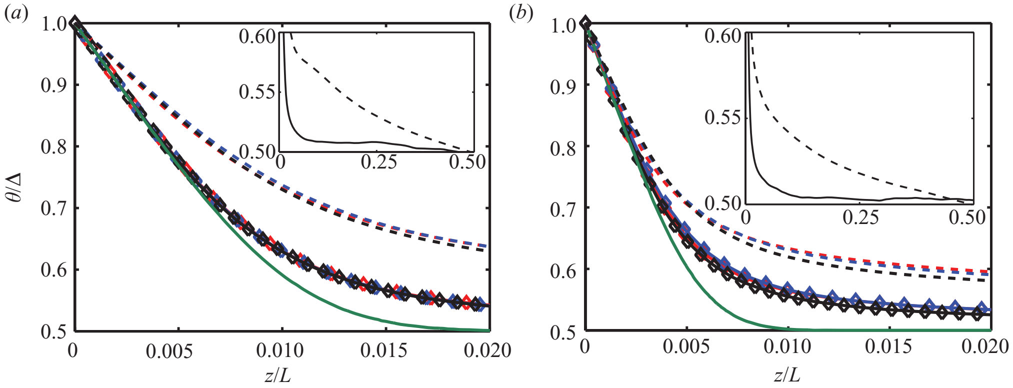

FIGURE 5. The azimuthally averaged temperature profiles obtained from the simulations at different grids. (*a*) $Ra = 2 \times 10^8$, for the grids $97 \times 49 \times 193$ (red), $193 \times 65 \times 257$ (blue) and $257 \times 97 \times 385$ (black) and (*b*) $Ra = 2 \times 10^9$ for the grids $129 \times 65 \times 257$ (red), $193 \times 65 \times 257$ (blue) and $385 \times 97 \times 385$ (black). The solid lines show the temperature profile at the cylinder axis ($r = 0$), the diamonds indicate the data points obtained from the simulation, and the dashed lines show the temperature profile at the radial position $0.225L$. The green line indicates the PB profile matched to the temperature gradient at the cylinder axis ($r = 0$) of the high-resolution simulation. The insets show the temperature profile from the highest resolution data over a larger axial range. Here the solid line indicates the profile at the axis and the dashed line the temperature profile at the radial position $0.225L$.

simulations. The temperature gradient of the PB profile is matched to the temperature gradient obtained in the high-resolution simulation. The temperature profile obtained in the simulations best matches the PB profile around the cylinder axis ($r = 0$). Close to the sidewall the agreement is worse because of the rising (falling) plumes in this region. We therefore compare the difference between the PB profile and the result obtained from the simulation for different values of Ra. We determine, at the cylinder axis, $(\theta_{sim} - \theta_{PB})/(\Delta - \theta_{PB})$ for the bottom BL and $(\theta_{PB} - \theta_{sim})/(\theta_{PB})$ for the top BL. Here θ_{sim} is the mean temperature at a distance λ_θ^{sl} from the plate and θ_{PB} the temperature according to PB at this height, after having matched the gradient at the

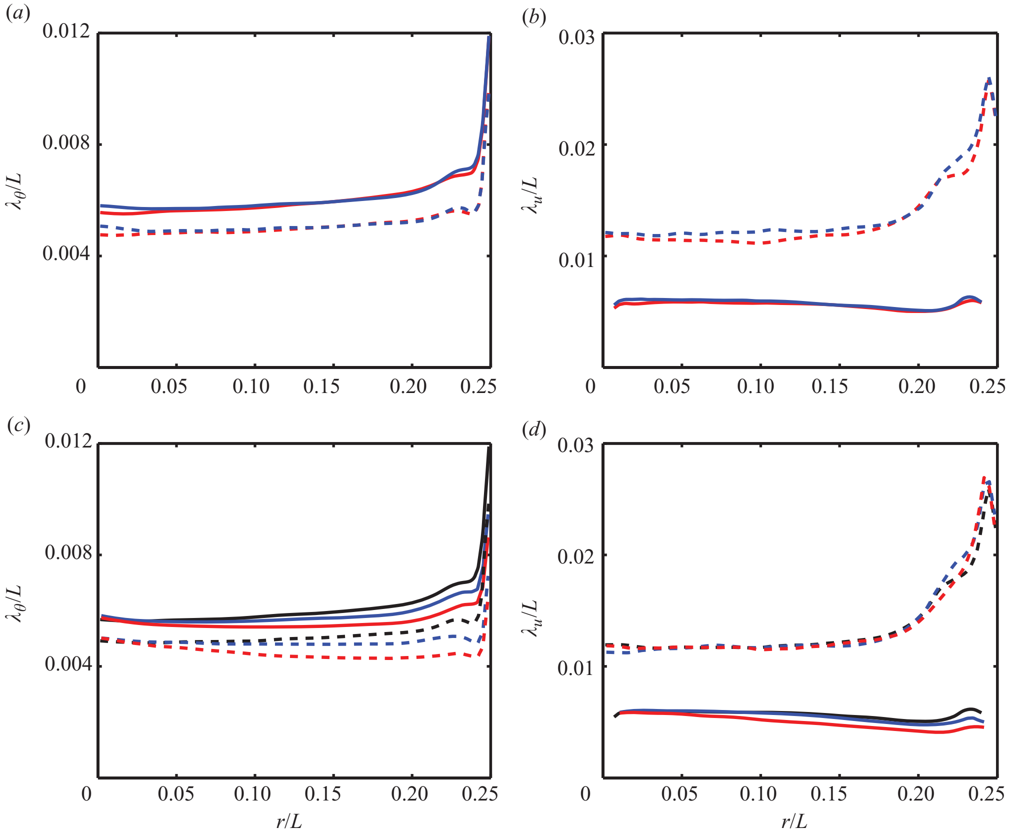

FIGURE 6. The azimuthally averaged BL thicknesses as a function of the radial position for $Ra = 2 \times 10^9$: (*a*) and (*b*) show the data from the high-resolution simulation ($385 \times 97 \times 385$). (*a*) The solid line indicates λ_θ^{sl}, and the dashed lines indicate λ_θ^{rms}, where red and blue indicate the bottom and top plates, respectively. (*b*) The solid line indicates $\lambda_u^{\epsilon_u}$ and the dashed line λ_u^{rms}, based on the azimuthal velocity (colours as in panel *a*). (*c*) Now the colours indicate the different grid resolutions: red, $129 \times 65 \times 257$; blue, $193 \times 65 \times 257$; and black, $385 \times 97 \times 385$. The solid lines indicate λ_θ^{sl} and the dashed lines λ_θ^{rms}. The data for the bottom and top BLs are averaged for clarity. Note that the BL is thicker (especially close to the sidewall) in the higher-resolution simulations, which is in agreement with the observed Nu trend. (*d*) The solid lines indicate $\lambda_u^{\epsilon_u}$ and the dashed lines λ_u^{rms}, based on the azimuthal velocity for the different grid resolutions (colours as in figure 6*c*).

plate to the simulation data. If the simulation exactly matched PB (e.g. for very small Ra), this expression would be zero. In contrast 0.103 (0.130, 0.149) is obtained for $Ra = 2 \times 10^8$ (2×10^9, 2×10^{10}). As expected, the expression is smaller for the lower Ra numbers. We perform the same procedure for our previous results of Zhong *et al.* (2009) at $Ra = 1 \times 10^8$ with $\Gamma = 1$ and now different Pr. For $Pr = 0.7$, $Pr = 6.4$ and $Pr = 20$ we now obtain 0.099, 0.040, and 0.033, respectively. Now the expression is closest to zero at the highest Pr, where the Re number of the flow is lowest, and thus the flow better fulfils the assumptions of the PB approximation. The agreement with the PB profile becomes less when the distance from the plate is larger because of the rising (falling) plumes in this region. This phenomenon is discussed in detail by Sugiyama *et al.* (2009).

Figure 6 shows the radial dependence of λ_θ^{sl}, λ_θ^{rms} – thermal BL thickness based on maximum root mean square (r.m.s.) value. First we determined the kinetic BL thickness by looking at λ_u^{rms} (kinetic BL thickness based on maximum azimuthal r.m.s. velocity). Although this definition is widely used in the literature it is clear that it overestimates the kinetic BL thickness because for $Pr = 0.7$ the kinetic BL thickness is smaller than the thermal BL thickness. One can see this in figure 2, where the BL region, indicated in red, is smaller for the kinetic BL than for the thermal BL. Therefore we also determine the kinetic BL thickness by looking at the axial profile of the kinetic energy dissipation. We define $\lambda_u^{\epsilon_u}$ (kinetic BL thickness defined as the axial position of the maximum kinetic energy dissipation rate, multiplied by 2) because this definition selects the region in which the kinetic dissipation is highest, and it is this region in which a particularly good resolution is required. Such defined kinetic BL thickness now well agrees with that of the thermal BL, $\lambda_u^{\epsilon_u} \approx \lambda_\theta^{sl}$, as expected from the PB theory for $Pr \approx 1$. Figure 6 shows that for both definitions the kinetic BL becomes thicker closer to the sidewall. This is due to the plumes travelling along the sidewall and lower velocities very close to the sidewall. We note that very close to the sidewall the definition of $\lambda_u^{\epsilon_u}$ therefore misrepresents the BL thickness. Thus the enhanced grid resolution in the vertical direction near the plates is most important around the cylinder axis ($r = 0$). In contrast, the azimuthal (and radial) resolution is most important to properly resolve the flow close to the sidewall. Note that the difference in the BL thicknesses between the fully resolved and under-resolved simulations is largest close to the sidewall, demonstrating that this is indeed a delicate region from a resolution point of view.

5. Conclusions

In summary, results from DNS with sufficient resolution using constant-temperature boundary conditions for the horizontal plates are in good agreement with the experimental data (see figure 1). Previous DNS results showed a Nusselt number that was up to 30 % higher than the experimental results. The new simulations have been performed with much higher resolution than the previous simulations to properly resolve the plume dynamics. Because in under-resolved simulations the hot (cold) plumes travel further from the bottom (top) plate than in the better-resolved ones, due to insufficient thermal dissipation close to the sidewall (where the grid cells are largest), the Nusselt number is overestimated in under-resolved simulations. It thus is crucial to properly resolve the plume dynamics to accurately determine the Nusselt number, and based on the simulations we have defined the resolution criteria that have to be fulfilled to have a fully resolved DNS. When the simulation is not fully resolved the exact relation $\epsilon_\theta = \kappa \Delta^2 Nu/L^2$ for the thermal dissipation rate does not hold. This is because the temperature gradients are smeared out in under-resolved simulations, leading to an underestimation of the thermal dissipation rate. We also showed that there is a strong radial dependence of the BL structures. At the cylinder axis ($r = 0$) the temperature profile obtained in the simulations agrees well with the PB case, whereas close to the sidewall the agreement is worse because of rising (falling) plumes in this region.

The effect of changing the constant-temperature condition at the bottom plate to a constant-heat-flux condition will be discussed in detail in a forthcoming publication.

We thank S. Grossmann and G. Ahlers for discussions and G. W. Bruggert for drawing figure 1(*b*). The work in Twente was supported by FOM and the National Computing Facilities (NCF), both sponsored by NWO. The simulations up to $Ra = 2 \times 10^{10}$ on the $513 \times 129 \times 513$ grid were performed on the Huygens cluster (SARA). The simulation at $Ra = 2 \times 10^{10}$ on the $385 \times 257 \times 1025$ grid and the $Ra=2\times10^{11}$ simulations were performed at the computing centre CASPUR in Roma. Support from Drs F. Massaioli and G. Amati is gratefully acknowledged.

REFERENCES

Ahlers, G., Grossmann, S. & Lohse, D. 2009 Heat transfer and large scale dynamics in turbulent Rayleigh–Bénard convection. *Rev. Mod. Phys.* **81**, 503.

Amati, G., Koal, K., Massaioli, F., Sreenivasan, K. R. & Verzicco, R. 2005 Turbulent thermal convection at high Rayleigh numbers for a constant-Prandtl-number fluid under Boussinesq conditions. *Phys. Fluids* **17**, 121701.

Castaing, B., Gunaratne, G., Heslot, F., Kadanoff, L., Libchaber, A., Thomae, S., Wu, X. Z., Zaleski, S. & Zanetti, G. 1989 Scaling of hard thermal turbulence in Rayleigh–Bénard convection. *J. Fluid Mech.* **204**, 1–30.

Chavanne, X., Chilla, F., Castaing, B., Hebral, B., Chabaud, B. & Chaussy, J. 1997 Observation of the ultimate regime in Rayleigh–Bénard convection. *Phys. Rev. Lett.* **79**, 3648–3651.

Chavanne, X., Chilla, F., Chabaud, B., Castaing, B. & Hebral, B. 2001 Turbulent Rayleigh–Bénard convection in gaseous and liquid He. *Phys. Fluids* **13**, 1300–1320.

Emran, M. S. & Schumacher, J. 2008 Fine-scale statistics of temperature and its derivatives in convective turbulence. *J. Fluid Mech.* **611**, 13–34.

Funfschilling, D., Bodenschatz, E. & Ahlers, G. 2009 Search for the 'ultimate state' in turbulent Rayleigh–Bénard convection. *Phys. Rev. Lett.* **103**, 014503.

Funfschilling, D., Brown, E., Nikolaenko, A. & Ahlers, G. 2005 Heat transport by turbulent Rayleigh–Bénard convection in cylindrical cells with aspect ratio one and larger. *J. Fluid Mech.* **536**, 145–154.

Grossmann, S. & Lohse, D. 2000 Scaling in thermal convection: a unifying view. *J. Fluid. Mech.* **407**, 27–56.

Grossmann, S. & Lohse, D. 2001 Thermal convection for large Prandtl number. *Phys. Rev. Lett.* **86**, 3316–3319.

Grossmann, S. & Lohse, D. 2002 Prandtl and Rayleigh number dependence of the Reynolds number in turbulent thermal convection. *Phys. Rev.* E **66**, 016305.

Grötzbach, G. 1983 Spatial resolution for direct numerical simulations of Rayleigh–Bénard convection. *J. Comput. Phys.* **49**, 241–264.

Heslot, F., Castaing, B. & Libchaber, A. 1987 Transition to turbulence in helium gas. *Phys. Rev.* A **36**, 5870–5873.

Johnston, H. & Doering, C. R. 2009 Comparison of turbulent thermal convection between conditions of constant temperature and constant flux. *Phys. Rev. Lett.* **102**, 064501.

Kaczorowski, M. & Wagner, C. 2009 Analysis of the thermal plumes in turbulent Rayleigh–Bénard convection based on well-resolved numerical simulations. *J. Fluid. Mech.* **618**, 89–112.

Kraichnan, R. H. 1962 Turbulent thermal convection at arbitrary Prandtl number. *Phys. Fluids* **5**, 1374–1389.

Kunnen, R. P. J., Clercx, H. J. H., Geurts, B. J., Bokhoven, L. J. A., Akkermans, R. A. D. & Verzicco, R. 2008 A numerical and experimental investigation of structure function scaling in turbulent Rayleigh–Bénard convection. *Phys. Rev.* E **77**, 016302.

Lohse, D. & Toschi, F. 2003 The ultimate state of thermal convection. *Phys. Rev. Lett.* **90**, 034502.

Lohse, D. & Xia, K. Q. 2010 Small-scale properties of turbulent Rayleigh–Bénard convection. *Annu. Rev. Fluid Mech.* **42**, 335–364.

Niemela, J., Skrbek, L., Sreenivasan, K. R. & Donnelly, R. 2000 Turbulent convection at very high Rayleigh numbers. *Nature* **404**, 837–840.

Niemela, J., Skrbek, L., Sreenivasan, K. R. & Donnelly, R. J. 2001 The wind in confined thermal turbulence. *J. Fluid Mech.* **449**, 169–178.

Niemela, J. & Sreenivasan, K. R. 2003 Confined turbulent convection. *J. Fluid Mech.* **481**, 355–384.

Nikolaenko, A., Brown, E., Funfschilling, D. & Ahlers, G. 2005 Heat transport by turbulent Rayleigh–Bénard convection in cylindrical cells with aspect ratio one and less. *J. Fluid Mech.* **523**, 251–260.

Roche, P. E., Castaing, B., Chabaud, B. & Hebral, B. 2002 Prandtl and Rayleigh numbers dependences in Rayleigh–Bénard convection. *Europhys. Lett.* **58**, 693–698.

SCHUMACHER, J., SREENIVASAN, K. R. & YEUNG, P. K. 2005 Very fine structures in scalar mixing. *J. Fluid. Mech.* **531**, 113–122.

SHANG, X. D., TONG, P. & XIA, K.-Q. 2008 Scaling of the local convective heat flux in turbulent Rayleigh–Bénard convection. *Phys. Rev. Lett.* **100**, 244503.

SHISHKINA, O. & WAGNER, C. 2007 Local heat fluxes in turbulent Rayleigh–Bénard convection. *Phys Fluids.* **19**, 085107.

SHISHKINA, O. & WAGNER, C. 2008 Analysis of sheetlike thermal plumes in turbulent Rayleigh–Bénard convection. *J. Fluid Mech.* **599**, 383–404.

SHRAIMAN, B. I. & SIGGIA, E. D. 1990 Heat transport in high-Rayleigh number convection. *Phys. Rev.* A **42**, 3650–3653.

SPIEGEL, E. A. 1971 Convection in stars. *Annu. Rev. Astron. Astrophys.* **9**, 323–352.

SUGIYAMA, K., CALZAVARINI, E., GROSSMANN, S. & LOHSE, D. 2009 Flow organization two-dimensional in non-Oberbeck–Boussinesq Rayleigh–Bénard convection in water. *J. Fluid Mech.* **637**, 105–135.

VERZICCO, R. & CAMUSSI, R. 1999 Prandtl number effects in convective turbulence. *J. Fluid Mech.* **383**, 55–73.

VERZICCO, R. & CAMUSSI, R. 2003 Numerical experiments on strongly turbulent thermal convection in a slender cylindrical cell. *J. Fluid Mech.* **477**, 19–49.

VERZICCO, R. & ORLANDI, P. 1996 A finite-difference scheme for three-dimensional incompressible flow in cylindrical coordinates. *J. Comput. Phys.* **123**, 402–413.

VERZICCO, R. & SREENIVASAN, K. R. 2008 A comparison of turbulent thermal convection between conditions of constant temperature and constant heat flux. *J. Fluid Mech.* **595**, 203–219.

ZHONG, J.-Q., STEVENS, R. J. A. M., CLERCX, H. J. H., VERZICCO, R., LOHSE, D. & AHLERS, G. 2009 Prandtl-, Rayleigh-, and Rossby-number dependence of heat transport in turbulent rotating Rayleigh–Bénard convection. *Phys. Rev. Lett.* **102**, 044502.